Eulerian and Lagrangian time scales of the turbulence above staggered arrays of cubical obstacles

Annalisa Di Bernardino[1] • Paolo Monti[1] • Giovanni Leuzzi[1] • Giorgio Querzoli[2]

[1] DICEA, Università di Roma “La Sapienza”, Via Eudossiana 18, 00184 Roma, Italy.
[2] DICAAR, Università degli Studi di Cagliari, Via Marengo 2, 09123 Cagliari, Italy.

Corresponding author:
Paolo Monti, E-mail: paolo.monti@uniroma1.it; Tel.: +390644585045
ORCID: 0000-0001-5194-1351

Annalisa Di Bernardino. ORCID: 0000-0003-3765-2179
Giovanni Leuzzi. ORCID: 0000-0003-3929-6737
Giorgio Querzoli. ORCID: 0000-0003-3770-6034

Abstract

We present results from water-channel experiments on neutral turbulent flows over arrays of cubical obstacles modelling idealised urban canopies with three different plan area fractions λ_P (0.1, 0.25 and 0.4). Attention is concentrated on the analysis of the vertical profiles of the Eulerian (T^E) and Lagrangian (T^L) time scales of the turbulence above the canopy. The results show that both the streamwise and vertical components of T^L increase approximately linearly with height above the obstacles, leading support to Raupach's linear law. The comparison with the Lagrangian time scales over two-dimensional roughness in the regimes of skimming flow and wake interference shows that the three-dimensionality of the canopy increases the streamwise T^L while decreasing its vertical counterpart. Furthermore, the assumption usually adopted on flat terrain that T^L/T^E is proportional to the inverse of the turbulence intensity holds true for all the three arrays. A good agreement has also been found between the eddy viscosities (K_T) estimated by applying Taylor's theory and the classical first order closure relating the momentum flux to the velocity gradient. The results also show that K_T obeys Prandtl's theory, particularly for $\lambda_P = 0.25$ and 0.4.

Keywords Building • Eddy diffusivity • Feature tracking • Raupach law • Urban canopy • Water channel

1 Introduction

In a previous paper (Di Bernardino et al. 2017 [1], henceforth D17), we presented detailed measurements on Lagrangian and Eulerian statistics of the velocity field obtained from a water-channel experiment mimicking the wind flow above idealised two-dimensional (2D) urban canyons. One of the objectives was to quantify the Eulerian (T^E) and Lagrangian (T^L) time scales of the turbulence as well as to investigate their dependence on the aspect ratio of the canyon, AR=W/H, as the latter is the ratio of the street width (W) to the height (H) of the canopy. Such a study is important since T^L is one of the main parameters required by Lagrangian models of turbulent dispersion [2]. These can be easily coupled with common Reynolds-averaged Navier-Stokes (RANS) models that, however, do not compute T^L, which is generally estimated from parametric laws applicable only over flat terrain.

The Lagrangian time scale of the turbulence is defined as the time integral of the Lagrangian autocorrelation function of the velocity, $\rho^L(\tau)$, viz.:

$$T^L = \int_0^\infty \rho^L(\tau)d\tau \tag{1}$$

and gives a rough measure of the time taken by a fluid particle to become decorrelated with its initial state (here τ is the time lag.). D17 found that within the inertial layer (also known as to the constant flux layer, CFL) over flat terrain, both the streamwise and vertical components of the Lagrangian time scales, T_u^L and T_w^L, follow Raupach's (1989) [3] linear law, originally derived for one-dimensional turbulent flows:

$$\frac{T_w^L u_{*,ref}}{\delta} = \frac{k}{([\sigma_w/u_*]_{ref})^2}\,\frac{z}{\delta} \tag{2}$$

where k=0.41 is the von Karman constant, z the height, δ the boundary-layer height, $u_{*,ref}$ and $\sigma_{w,ref}$ the reference values (i.e. averaged within the CFL) of the friction velocity and the standard deviation of the vertical velocity component, respectively. The expression for $T_u^L u_{*,ref}/\delta$ is identical to Eq. (2) but with $\sigma_{u,ref}$ in place of $\sigma_{w,ref}$, where the former is the reference value of the standard deviation of the streamwise velocity component. Equation (2) was obtained by matching the expressions of the linear growth with height of the eddy diffusivity of momentum based on the Prandtl mixing-length theory, $K_T = ku_* z$, and the far-field eddy diffusivity, $K_T = \sigma_w^2 T_w^L$ [4].

D17 found a reasonable agreement between T_u^L, T_w^L and Eq. (2) also for their two-dimensional canopy flows, except for T_u^L when AR=2 (wake-interference regime, see below), which differed considerably from T_w^L for $z/H \lesssim 2$, i.e. within the roughness sublayer (RSL) and the lower part of the CFL. The former is the portion of boundary layer immediately above the canopy where the flow is non-homogenous and strongly influenced by the roughness elements constituting the canopy (see e.g. [5]). In that case, H can be used as length scale in place of δ and the distance from the bottom on the right-hand term of the equation is lowered by the displacement height, d. Note that Raupach's law is a simple expression whose terms can be obtained from routine one-point measurements.

Due to the growing interest of the scientific community in predicting wind flow and pollutant dispersion in more common, three-dimensional (3D) urban canopies – see recent experimental (e.g. [6-9]) and numerical (e.g. [10-13]) works on the subject –, we used the same water-channel apparatus described by D17 to investigate the turbulent flow above staggered arrays of cubical obstacles. Three experimental arrangements are considered for the analysis as a function of the plan area fraction, $\lambda_P = A_P/A_T$, i.e. the ratio of the plan area of roughness elements to the total surface area. In particular, the first arrangement, $\lambda_P = 0.1$, refers to the isolated-flow regime ($\lambda_P < 0.13$), where the interaction between individual building wakes is weak; the second, $\lambda_P = 0.25$, corresponds to the wake-interference regime ($0.13 < \lambda_P < 0.35$), in which the spacing between buildings is close enough that the wakes strengthen each other; while the third, $\lambda_P = 0.4$, belongs to the skimming flow regime, i.e. when the obstacles are so packed that the outer flow skips over their tops ($\lambda_P > 0.35$) (see e.g. [14]).

Whilst the wake-interference regime has been widely studied in the literature, in particular the case $\lambda_P = 0.25$, which is practically assumed as an archetype for 3D building arrays ([15-18], among others), less attention has been paid to the other two regimes (see e.g. [19-21]), even though both belong to the range of plan area fractions typically found in real cities [22]. After a brief description of the experimental setup and data analysis (Sec. 2), the paper reports Lagrangian and Eulerian statistics of the flow (Sec. 3), paying also attention to the differences or similarities with the 2D case investigated by D17. In addition, information is given on an additional parameter of interest for dispersion processes such as the turbulent diffusivity of momentum. The final remarks are drawn in Sec. 4.

2 Experimental Setup and Data Analysis

The experiments were conducted in the recirculating water channel of the Hydraulic Laboratory of the University of Rome – La Sapienza, Italy. Since the velocity measurement technique and data processing have already been described in D17 and [23], only the salient features of the experimental setup are briefly reviewed here. The channel (7.4 m long) has a rectangular cross section 0.35 m high and 0.25 m wide. To observe the flow visually, the lateral sides of the tank are made of transparent glass. The flume is fed by a constant head reservoir. The neutral atmospheric boundary layer is recreated increasing the roughness of the channel bottom via randomly distributed pebbles with average diameter ≈ 5 mm. The water depth and the free-stream velocity are 0.16 m and U=0.34 m s^{-1}, respectively. The roughness length of the surface, z_0, is estimated by fitting the usual logarithmic law form of the velocity, $\bar{u} = u_{*,ref} k^{-1} \ln[(z-d)/z_0]$, to the measurements in the constant flux region, where $u_{*,ref} = 0.017\ \mathrm{ms}^{-1}$ is the reference friction velocity and the bar indicates the time average. A satisfactory fit is found for d=0 and $z_0 = 0.3$ mm, i.e. nearly 0.06 times the average pebble diameter (see D17 for details regarding the characteristics of the approaching flow).

The roughness Reynolds number, $Re_\tau = u_{*,ref} H/\nu$, ranges from 300 to 360 ($\nu = 10^{-6}\ \mathrm{m^2 s^{-1}}$ is the kinematic viscosity of water) and it is well above the critical value, ensuring that both the large-scale turbulence and the mean flow can be assumed as being independent of Reynolds [24].

Each array of obstacles is designed by means of uniform, sharp-edged cubes with height H=15 mm glued onto the channel bottom in staggered pattern (Fig. 1). Details of the three arrays are given in Tab. 1 and Fig. 2.

	$\lambda_P = 0.1$	$\lambda_P = 0.25$	$\lambda_P = 0.4$
Element distance (mm, see Fig. 2)	32	15	9
Unit size (mm^2)	47	30	24

Table 1 Geometrical characteristics of the three building arrays

In order to analyse both the Eulerian and Lagrangian characteristics of the flow, two different acquisition setups were considered. In particular, the Eulerian variables were measured on a rectangular area lying in the vertical x–z plane (0.11 m long and 0.055 m high), parallel to the streamwise direction and passing through the centre of the channel (see green lines in Fig. 2). The measurement area was illuminated by a thin light sheet (≈2 mm thick) from a 5 W green laser and the water was seeded with neutrally buoyant particles (≈2 μm in diameter), assumed as being transported passively by the flow. Each experiment consisted of a set of N=10,000 images acquired by means of a video camera (250 Hz, 1280x1024 pixels in resolution).

Velocity fields were obtained using a feature tracking technique, which recognises particle trajectories and deduces velocities from particle displacements between successive frames.

Velocity evaluation:

The feature tracking algorithm is based on the assumption of the invariance of particle images (the so-called features) between successive frames (Cenedese et al., 2005). As a consequence, the tracking problem can be posed as the minimization of the residue (Lucas and Kanade, 1981):

$$\varepsilon = \int_W \left(\frac{\partial I(\boldsymbol{x}, t)}{\partial t} + \nabla I(\boldsymbol{x}, t)\boldsymbol{u} \right)^2 dW$$

where I indicates the light intensity on the image and $\boldsymbol{u}$ the particle velocity. In order to ε to be a minimum, the derivatives of the residue with respect to the velocity components must be set to zero, thus yielding a set of two equations where the two velocity components are the unknowns:

$$G\boldsymbol{u} = \boldsymbol{e}$$

where:

$$G = \int_W \begin{bmatrix} \left(\frac{\partial I}{\partial x}\right)^2 & \left(\frac{\partial I}{\partial x}\frac{\partial I}{\partial y}\right) \\ \left(\frac{\partial I}{\partial x}\frac{\partial I}{\partial y}\right) & \left(\frac{\partial I}{\partial y}\right)^2 \end{bmatrix} dW$$

and

$$\boldsymbol{e} = \int_W \frac{\partial I}{\partial t} \begin{bmatrix} \frac{\partial I}{\partial x} \\ \frac{\partial I}{\partial y} \end{bmatrix} dW$$

Particle recognition:

The tracking problem, i.e. the above set of linear equations, can be solved reliably provided that both the eigenvalues of G, computed over the interrogation window W, are about of the same order of magnitude and not too small compared to the image noise level. In practice, we use a threshold criterion on the second (minimum) eigenvalue: firstly we compute the eigenvalues of G for every possible window over the image; secondly we look for local maxima of the minimum eigenvalue and, thirdly, we accept a window, W, as a valid particle (a "good feature to track" (Shi and Tomasi, 1994)) provided the second eigenvalue, *i*) is a local maximum; *ii*) exceeds an assigned threshold value, *iii*) there are no other local maxima with higher value within an assigned radius, r_{min} (chosen to be larger than the typical particle size). As a matter of fact, high eigenvalues are found in the region of the image the where spatial gradients of the luminosity are elevated. Therefore, local maxima corresponded, in our images, to the bright spots left by the seeding particles. The third condition avoids multiple recognitions of the same particle.

Trajectory recognition:

The particle recognition and tracking procedures described above where combined to recognize particle trajectories using the typical strategy of PTV algorithms. At each instant, the next position of the existing trajectories was predicted using the velocity evaluation algorithm described above. The position is validated by means of a minimum eigenvalue threshold criterion. After the existing trajectories are continued, the present image is searched for new features using the particle recognition algorithm. In order to avoid multiple recognitions of the same particle, a new feature is accepted only if the minimum distance from other validated features exceeds a given threshold, r_{min}. In order to minimize possible trajectory recognition errors and consequent spurious velocity samples, a trajectory is assumed valid only if the particle is tracked for at least two consecutive time instants.

Eulerian statistics

In order to compute the Eulerian statistics, a Gaussian interpolation algorithm was applied to the scattered data so as to obtain the instantaneous velocity fields on a regular grid [25]. The so-obtained results have a spatial resolution of 1 mm and a temporal resolution of 1/250 s. Additional experiments were also conducted framing the free surface to evaluate the free-stream velocity and the turbulent boundary-layer depth.

The statistics of the Eulerian velocity fields were obtained by time averaging over the N time instants. We calculated the mean velocity components $\bar{u}(m,n)$ and $\bar{w}(m,n)$, the variances $\sigma_u^2(m,n) = \overline{u'^2}(m,n)$ and $\sigma_w^2(m,n) = \overline{w'^2}(m,n)$ as well as the vertical momentum flux $\overline{u'w'}(m,n)$ at each node (m,n) of the 110 (along x) x 55 (along z) grid (the prime is the fluctuation around the mean).

The Eulerian time scales for the velocity component along the *j*-th axis is:

$$T_j^E = \int_0^\infty \rho_j^E(\tau)d\tau = \int_0^\infty \frac{\overline{v_j{}'(t)v_j{}'(t+\tau)}}{\sigma_j^2}d\tau \qquad (3)$$

where $\rho_j^E(\tau)$ is the Eulerian autocorrelation function of the *j*-th velocity component and t the time.

Lagrangian statistics

To reconstruct the particle trajectories needed for the determination of the Lagrangian time scales of the flow, a second set of experiments were conducted in the same flow conditions but changing the acquisition setup so that the longest possible trajectories could be acquired. To this aim, the framed area was 0.30x0.15 m^2 and the flow was illuminated by a light sheet 0.02 m thick generated by a 1000 W, white halogen lamp. The increased thickness of the light sheet ensures that only a negligible fraction of the trajectories was truncated because of spanwise displacement. The seeding density was correspondingly decreased in order to have a few particle at the same time in the illuminated volume and thus minimize the ambiguity due to the superimposition of particles at different depths despite of the light sheet increase. Each experiment consisted of ≈100,000 images, sampled at a 500 Hz frame rate.

The Lagrangian time scales were calculated from the set of particle trajectories detected during the image-processing procedure that where long at least 350 instants (corresponding to 0.7 s). Results presented below show that the minimum length is significantly larger than the turbulence time scale in all the configurations. The total number of trajectories exceeding the requested length during each experiment is reported in Tab. 2.

	$\lambda_P = 0.1$	$\lambda_P = 0.25$	$\lambda_P = 0.4$
Number of trajectories	129,801	161,259	135,950

Table 2 Number of trajectories exceeding the minimum length (350 instants)

Let us assume that the tracking of the k-th particle starts at reference time $t_0^{(k)}$ and reference position $\boldsymbol{x}_0^{(k)}$. We indicate its position and velocity at a generic time by $\boldsymbol{X}^{(k)}\left(\boldsymbol{x}_0^{(k)}, t_0^{(k)}, t\right)$ and $\boldsymbol{U}^{(k)}\left(\boldsymbol{x}_0^{(k)}, t_0^{(k)}, t\right)$, respectively (letters in capital refer to Lagrangian properties, while bold indicates vector quantities). Furthermore, provided the phenomenon is statistically steady in a Eulerian sense, averages are independent of the reference time $t_0^{(k)}$. However, they still depend on the time lag, $\tau = t - t_0^{(k)}$, and reference position $\boldsymbol{x}_0^{(k)}$. Consequently, the Lagrangian average velocity can be written as:

$$\langle \boldsymbol{U} \rangle(\boldsymbol{x}_0, \tau) = \frac{1}{M_{\boldsymbol{x}_0}} \sum_{k|_{x_0}} \boldsymbol{U}^{(k)}\,(\boldsymbol{x}_0, \tau) \tag{4}$$

where the summation refers to the $M_{\boldsymbol{x}_0}$ trajectories starting from $\boldsymbol{x}_0$. Similarly, the standard deviation of the j-th component of the velocity is computed as:

$$\sigma_j^L(\boldsymbol{x}_0, \tau) = \sqrt{\frac{1}{M_{\boldsymbol{x}_0}} \sum_{k|_{x_0}} \left[U_j^{(k)}(\boldsymbol{x}_0, \tau) - \langle U_j \rangle(\boldsymbol{x}_0, \tau)\right]^2} \tag{5}$$

while the auto-correlation coefficient is expressed as:

$$\rho_j^L(\boldsymbol{x}_0, \tau) = \frac{1}{M_{\boldsymbol{x}_0}} \frac{\sum_{k|_{x_0}} \left\{\left[U_j^{(k)}(\boldsymbol{x}_0, \tau) - \langle U_j \rangle(\boldsymbol{x}_0, \tau)\right]\left[U_j^{(k)}(\boldsymbol{x}_0, 0) - \langle U_j \rangle(\boldsymbol{x}_0, 0)\right]\right\}}{\sigma_j^L(\boldsymbol{x}_0, \tau)\sigma_j^L(\boldsymbol{x}_0, 0)} \tag{6}$$

The Lagrangian time scale of the j-th velocity component, T_j^L, is evaluated as the integral of the corresponding Lagrangian autocorrelation function, viz.:

$$T_j^L(\boldsymbol{x}_0) = \int_0^\infty \rho_j^L(\boldsymbol{x}_0, \tau) d\tau \tag{7}$$

The ratio between the Lagrangian and the Eulerian time scales can be expressed (Corrsin 1963 [26]) as equal to a proportionality constant β (greater than unity):

$$\beta = T^L / T^E = \gamma / i \tag{8}$$

where i is the turbulence intensity and γ is a proportionality constant of order one. Although Eq. (8) should, in principle, be valid only for isotropic turbulence, it has also been used in inhomogeneous turbulence (see e.g. [27]). More discussion on the methods of calculation of the integral scales of the turbulence can be found in [28] and [29].

Finally, we will also focus on the spatial autocorrelation functions of both the streamwise and vertical velocity components, viz.

$$R_u(\boldsymbol{x_0}, \boldsymbol{r}) = \frac{\overline{u'(\boldsymbol{x_0})u'(\boldsymbol{x_0}+\boldsymbol{r})}}{\sigma_u(\boldsymbol{x_0})\sigma_u(\boldsymbol{x_0}+\boldsymbol{r})} \tag{9}$$

$$R_w(\boldsymbol{x_0}, \boldsymbol{r}) = \frac{\overline{w'(\boldsymbol{x_0})w'(\boldsymbol{x_0}+\boldsymbol{r})}}{\sigma_w(\boldsymbol{x_0})\sigma_w(\boldsymbol{x_0}+\boldsymbol{r})} \tag{10}$$

where $\boldsymbol{r}$ is the displacement relative to $\boldsymbol{x_0}$. The integrals of the above autocorrelations, performed along the streamwise direction, yield the integral length scales $L_{u,x}(\boldsymbol{x_0})$ and $L_{w,x}(\boldsymbol{x_0})$. These represent a measure of the distance along the horizontal direction over which the velocities are correlated. Turbulent length scales are useful tools for evaluating mixing properties of the boundary layer (see e.g. [30-33]), but their estimation in field campaigns is quite problematic since it requires multi-point velocity measurements [34].

3 Results and Discussion

Since we are interested in getting information on the flow characteristics above the building tops and given the flow three-dimensionality, an average of the variables over a sufficiently large number of individual sections belonging to different vertical planes parallel to the streamwise direction would be necessary to obtain representative spatially-averaged properties of the flow. However, to avoid very time-consuming experiments, it was decided to consider only the vertical section passing through the centre of the obstacles (see green lines in Fig. 2). With regard to previous issue, [35] showed that for a regular array of staggered cubical obstacles with $\lambda_P = 0.25$, no significant errors occur by considering only measurement points belonging to the vertical plane passing through the middle section of the obstacles. Note also that, as emphasised by those authors, such a simplification may be inappropriate for other geometrical arrangements, even though the regular dispositions of the cubes considered in our experiments might do not involve appreciable errors, particularly for $\lambda_P = 0.4$.

The vertical profiles of the Eulerian variables were estimated by adopting the canopy approach (e.g. [36]), namely by horizontally averaging the time averaged statistics over a region including one building top and the contiguous canyon. In doing so, the results can be assumed as representative of the repeating unit constituting the canopy, keeping in mind the limitation mentioned above.

3.1 Mean Velocity and Reynolds Stresses

Figure 3 shows the vertical profiles of the normalised streamwise velocity component (Fig. 3a), Reynolds shear stress (Fig. 3b) and standard deviation of the horizontal (σ_u) and vertical (σ_w) velocity components (Fig. 3c) for the three arrays. For $\lambda_P = 0.25$ (wake-interference regime), the profiles are quantitatively similar to those reported by other authors (see e.g. [35]). The Reynolds shear stress varies up to $z \approx 1.8H$ (i.e. the RSL depth), then it is independent on z up to $z/H \approx 3.2H$, which can be considered as the upper limit of the CFL (Fig. 3b). While the $\lambda_P = 0.4$ case (skimming flow) behaves similarly to $\lambda_P = 0.25$, for $\lambda_P = 0.1$ (isolated regime) the RSL is considerably deeper and the CFL forms at nearly $z \approx 2.8H$. This agrees with other observations conducted in the laboratory [32] and in the real field [37]. Note also that $\sigma_w/u_{*,ref}$ and $\sigma_u/u_{*,ref}$ do not change appreciably with height in the whole z/H range analysed, $\lambda_P = 0.1$ case showing slightly larger values, in agreement with [38].

The similarity found between $\lambda_P = 0.25$ and 0.4 is not surprising since in terms of classical roughness terminology the former can be considered as near the so called 'd-type' roughness - the same one to which the latter belongs - where the cavities sustain stable recirculating vortices that isolate the upper flow from the inner one. In contrast, lower λ_P are typical of 'k-type' roughness, where the distribution of the roughness elements is sparse and vortex shedding between the elements characterises the flow (see [39-40] and [11] for more discussion on this subject). Recent wind-tunnel results by [8] on the effect of building packing density on the drag force over aligned arrays of cubes show that the shear stress increases with increasing packing density up to $\lambda_P = 0.25$. The larger Reynolds shear stress we found for $\lambda_P = 0.1$ compared to $\lambda_P = 0.25$ and 0.4 therefore goes against [8]. On the other hand, direct numerical simulations by [38] conducted for staggered arrays of cubical obstacles (like those considered in our experiments) showed that the total shear stress peaks for lower packing density ($\lambda_P \approx 0.13$), not far from $\lambda_P = 0.1$. However, we must bear in mind that we considered only the vertical plane passing through the cube centre to measure the velocity field (see discussion at the beginning of the present section).

3.2 Eulerian Integral Time Scales

The Eulerian time scales for the streamwise and the vertical velocity components, T_u^E and T_w^E, respectively, are estimated using Eq. (3) considering the time at which the autocorrelation decreases to $1/e$ (here, e is the Euler number). This is a very common procedure for the extraction of integral time scales since the mathematical form of the autocorrelation is generally a decaying exponential [41]. The characteristic time $H/u_{*,ref}$ is used to normalise T_u^E and T_w^E.

Analysis of Fig. 4a indicates that: (*i*) overall, the three non-dimensional T_u^E (continuous lines with symbols) increase approximately linearly with height within the RSL, then they remain nearly constant in the overlying CFL (*ii*) T_u^E does not change appreciably passing from $\lambda_P = 0.25$ to $\lambda_P = 0.4$, even though, in the latter case, larger T_u^E at the top of the cavity are present (Fig. 4a) (*iii*) a strict resemblance between the two T_w^E for $\lambda_P = 0.25$ and 0.4 is apparent. In contrast, for $\lambda_P = 0.1$, T_w^E is everywhere larger, while T_u^E exceeds those found for $\lambda_P = 0.25$ and $\lambda_P = 0.4$ within the RSL.

The strict similarity between $\lambda_P = 0.25$ and 0.4 is furtherly corroborated by looking at the non-dimensional integral spatial scales (Fig. 4b), which are obtained by integrating the autocorrelations functions (Eqs. 9 and 10). In particular, by integrating along the streamwise direction Eq. (9) (Eq. 10), we calculate the integral length scale $L_{u,x}$ ($L_{w,x}$), which gives a measure of the distance along the horizontal direction over which the streamwise (vertical) velocity component is correlated with itself. As for the integral time scales, we obtain the vertical profiles of $L_{u,x}$ and $L_{w,x}$

moving $\boldsymbol{x_0}$ along the vertical axis passing through the centre of the cavity and evaluating the distance where the autocorrelation decreases to $1/e$. Both the scales reach an asymptotic value ($L_{u,x} \approx 2.7H$, $L_{w,x} \approx 0.9H$) within the CFL (Fig. 4b) and agree reasonably well with $L_{u,x} \approx 3H$ and $L_{w,x} \approx 1.2H$ found by [42]. Unfortunately, due to technical limitations, the case $\lambda_P = 0.1$ was not suitable for spatial autocorrelation estimate and, therefore, the corresponding spatial scales could not be determined.

The resemblance between skimming flow and wake-interference regime discernible from Eulerian scale analysis contrasts with the results of D17 for two-dimensional flows, where the dissimilarities between skimming flow and wake-interference regime were noticeable. For ease of comparison, Fig. 4a reports T_u^E and T_w^E estimated by D17 for aspect ratios AR=1 (dashed lines) and 2 (dotted lines). We see how AR=1 (corresponding to $\lambda_P = 0.5$, i.e. skimming flow) resembles skimming flow and wake-interference regime for the 3D case, while AR=2 (corresponding to $\lambda_P = 0.33$, i.e. wake-interference regime) is quite different from its 3D counterpart, showing larger T_u^E and T_w^E. This is understandable simply by considering the profound differences existing in 2D flows between those regimes both within and above the canopy [43-46]. This fact can be explained also in terms of different sizes of the coherent structures characterizing the two flows above the canopy (see [47] for a comprehensive discussion on that subject). Finally, the strict similarity between the T_w^E calculated for AR=2 and that obtained in 3D for the isolated flow ought to be just a coincidence in that no physical reason seems to support this result.

3.3 Lagrangian Integral Time Scales

Two-dimensional fields of ρ_u^L and ρ_w^L can be determined using Eq. (6) and considering all the trajectories starting in the proximity of each node of the Eulerian grid. However, given the quasi-horizontal homogeneity of the flow above the canopy, ρ_u^L and ρ_w^L are calculated following all the trajectories that begin in a horizontal fluid layer 1 mm thick, extended horizontally over the whole domain, passing through the nodes of the Eulerian grid. The resulting T_u^L and T_w^L are determined using Eq. (7) by considering the time lag when the autocorrelations decrease to $1/e$. As for the Eulerian scales, the characteristic time $H/u_{*,ref}$ is used to normalise T_u^L and T_w^L.

Like for their Eulerian counterparts, T_u^L and T_w^L do not change considerably going from $\lambda_P = 0.25$ to 0.4 (Figs. 5b and 5c). It is worthwhile to note also that for those two canopies $T_u^L \approx (2-3)T_w^L$ in the whole boundary layer analyzed, including the region near the top of the obstacles. The latter is a significant difference with the results of D17 for the 2D skimming flow (AR=1), where $T_u^L \approx T_w^L$ up to z=3H (red and blue lines in Fig. 5c). Overall, the 3D canopy tends to decrease the scale of the vertical velocity component while increasing the scale of the horizontal component as compared to the 2D case.

With regard to the wake-interference regime (Fig. 5b), a question arises regarding the T_u^L profile found for $1.5 < z/H < 2.5$ in that it is not clear how to interpret the observed nearly-constant values. However, a certain qualitative resemblance of T_u^L with the 2D case (red line) seems to occur, even though it decreases considerably approaching the top of the obstacles.

T_u^L estimated for $\lambda_P = 0.1$ (Fig. 5a) differs significantly from those calculated for $\lambda_P = 0.25$ and 0.4. Although both T_u^L and T_w^L increase roughly linearly in the whole boundary layer, their slopes are quite different and T_u^L increases much faster with height than T_w^L does. However, a reasonable agreement between T_w^L and Eq. (2) is found in all the three cases, in particular for $\lambda_P = 0.4$. The displacement heights used to test Eq. (2), i.e. d=0.56H, 0.78H and 0.93H for $\lambda_P = 0.1$, 0.25 and 0.4, respectively, have been calculated by means of the empirical law by [48].

It is worthwhile stressing here that Eq. (2) has been used in the past only for vegetation canopies (e.g. [49]) and 2D canopy flows [1] and, to our knowledge, this is the first time it has been tested in 3D urban canopy layers.

3.4 Lagrangian to Eulerian Time Scales Ratio

The vertical profiles of the Lagrangian to Eulerian integral scale ratio, β, are depicted in Fig. 6. The streamwise component, $\beta_u = T_u^L/T_u^E$ (solid diamonds), is always lower than the vertical one, $\beta_w = T_w^L/T_w^E$ (open diamonds), in agreement with the LES results of [27], who found $\beta_u = 5.09$ and $\beta_w = 10.24$ (values averaged over the whole boundary-layer depth in the case of flat terrain) and the 2D canopy flow by D17. β_u and β_w are always larger than unity, as generally expected in the presence of a mean flow [50].

The agreement found between T_w^L/T_w^E and γ/i_w (dashed line) and T_u^L/T_u^E and γ/i_u (continuous line) is quite good in all the three geometries, where $i_u = \sigma_u/\bar{u}$ and $i_w = \sigma_w/\bar{u}$ are the turbulence intensities and γ is a proportionality constant [26]. This is quite surprisingly given the assumption of isotropic flow field under which Corrsin (1963) [26] derived Eq. (8). This feature has not been reported in earlier vegetation or 3D urban canopy studies. In respect of the values of γ set in Eq. (8), it is worth noting that it falls in the range generally found in the literature (0.4-0.8) in the case of flows with small turbulent intensity.

3.5 Turbulent Diffusivity

We conclude the analysis by presenting in Fig. 7 the comparison of the vertical profiles of two estimations of the turbulent diffusivity, K_T. The first is based on the first-order closure for the momentum flux, $K_{T,fo} = -\overline{u'w'}d\bar{u}/dz$ (solid circles), while the second relies on Taylor's theory, $K_{T,T} = \sigma_w^2 T_w^L$ (open circles). Even though the former frequently fails in the presence of large eddies, it is commonly adopted in computational fluid dynamics. The agreement between the two is good both within and above the RSL (Fig. 7). In both the cases, they grow roughly linearly with height and are not far from the eddy diffusivity based on Prandtl's mixing-length theory, $K_{T,P} = ku_{*,ref}(z-d)$ (solid line), to be assumed valid in principle only within the CFL, where local equilibrium between momentum flux and wind gradient holds. This contrasts with what D17 found for the 2D canopies, where $K_{T,T}$ differed significantly from $K_{T,fo}$, particularly for the wake-interference regime. The less satisfactorily agreement observed for $\lambda_P = 0.25$, when $K_{T,T}$ deviates considerably from the other two determinations of K_T, is presumably associated with the anomalous behaviour of T_w^L found in the wake-interference regime.

We would have expected a better agreement of $K_{T,fo}$ and $K_{T,T}$ with Prandtl's mixing-length theory in the CFL rather than in the RSL since only in the former layer the logarithmic law is valid (see e.g. discussion in [51]). It should however be noted that the slopes of all the three formulations are very sensitive to values set for the von Karman constant and the reference friction velocity. For instance, by setting k=0.37 (a value within the range typically reported in the literature [52]) in place of 0.41 the slopes of the three formulations match in the CFL. In light of this, it stands to reason that Prandtl's mixing-length theory can be assumed as a realistic approximation for the eddy diffusivity of momentum above 3D canopies, at least for the skimming flow and the wake-interference regimes.

4 Concluding remarks

Results from water-channel experiments on the turbulent flow above arrays of staggered cubical obstacles mimicking idealised urban canopies for three different plan area fractions ($\lambda_P = 0.1$, 0.25 and 0.4) were presented. All the experiments refer to neutral conditions. Attention is focussed on the Lagrangian and Eulerian time scales of the turbulence and on the eddy diffusivity of momentum. The main findings include the following:

i) Although in the literature regular obstacle arrays with $\lambda_P = 0.25$ and 0.4 are considered belonging to different flow regimes (wake-interference and skimming flow, respectively), no substantial differences among all the measured quantities for the two cases appear above the top of the obstacles. This is understandable in that $\lambda_P = 0.25$ and 0.4 can be both classified as d-type roughness, where the exchanges of mass and momentum between inner and outer flow are small. In contrast, the case $\lambda_P = 0.1$ (isolated flow, classified as k-type roughness) behaves differently from the other two.

ii) Both the streamwise, T_u^L, and vertical, T_w^L, components of the Lagrangian time scale of the turbulence increase approximately linearly with the height within the whole boundary layer analysed (1<z/H<3), including the roughness sublayer and part of the constant flux layer that form above the canopy. Especially, to the best of our knowledge, this is the first time that experimental evidence on the agreement between T_w^L and Raupach's (1999) [3] law has been presented for 3D arrays of cubical obstacles.

iii) The agreement between T_w^L/T_w^E and γ/i_w and T_u^L/T_u^E and γ/i_u is pretty good in all the three geometries, where $i_u = \sigma_u/\bar{u}$ and $i_w = \sigma_w/\bar{u}$ are the turbulence intensities and γ is a proportionality constant.

iv) A reasonable agreement between the turbulent viscosities (K_T) calculated applying the first order closure and Taylor's theory holds both within and above the RSL. These estimations of K_T show a linear growth with height, in accordance with Prandtl's theory. This suggests that the latter, simple expression of K_T might be used with a certain degree of reliability, at least for $\lambda_P = 0.25$ and 0.4.

Acknowledgements This research was supported by the RG11715C7D43B2B6 fund from the University of Rome "La Sapienza". The assistance of Manuel Mastrangelo and Cristina Grossi (Master degree students of the University of Rome "La Sapienza") to the measurements was greatly appreciated.

References

1. Di Bernardino A, Monti P, Leuzzi G, Querzoli G (2017) Water-channel estimation of Eulerian and Lagrangian time scales of the turbulence in idealized two-dimensional urban canopies. Bound-Layer Meteorol 165:251–276
2. Thomson DJ (1987) Criteria for the selection of stochastic models of particle trajectories in turbulent flows. J Fluid Mech 180:529–556
3. Raupach MR (1989) Applying Lagrangian fluid mechanics to infer scalar source distributions from concentration profiles in plant canopies. Agric For Meteorol 47:85–108
4. Taylor GI (1921) Diffusion by continuous movements. Proc Lond Math Soc 20:196
5. Rotach MW (1999) On the influence of the urban roughness sublayer on turbulence and dispersion. Atmos Environ 33:4001–4008
6. Roth M, Inagaki A, Sugawara H, Kanda M (2015) Small-scale spatial variability of turbulence statistics, (co)spectra and turbulent kinetic energy measured over a regular array of cube roughness. Environ Fluid Mech 15:329-348
7. Nosek S, Kukačka L, Kellnerova R, Jurčàkovà K, Jaňour Z (2016) Ventilation processes in a three-dimensional street canyon. Bound-Layer Meteorol 159:259-284

8. Buccolieri R, Vigö H, Sandberg N, Di Sabatino S (2017) Direct measurements of the drag force over aligned arrays of cubes exposed to boundary-layer flows. Environ Fluid Mech 17:373-394

9. Monnier B, Goudarzi SA, Vinuesa R, Wark C (2018) Turbulent structure of a simplified urban fluid flow studied through stereoscopic particle image velocimetry. Bound-Layer Meteorol 166:239-268

10. Tomas JM, Eisma HE, Pourquie MJBM, Elsinga GE, Jonker HJJ, Westerweel J (2017) Pollutant dispersion in boundary layers exposed to rural-to-urban transitions: Varying the spanwise length scale of the roughness. Bound-Layer Meteorol 163: 225-251

11. Castro IP, Xie Z-T, Fuka V, Robins AG, Carpentieri M, Hayden P, Hertwig D, Coceal O (2017). Measurements and computations of flow in an urban street system. Bound-Layer Meteorol 162: 207-230.

12. Saeedi M, Wang B-C (2017) Large-eddy simulation of turbulent flow and structures within and above an idealized building array. Environ Fluid Mech 17:1127-1152

13. Goulart EV, Coceal O, Belcher SE (2018) Dispersion of a passive scalar within and above an urban street network. Bound-Layer Meteorol 166:351-366

14. Grimmond CSB, Oke TR (1999) Aerodynamic properties of urban areas derived from analysis of urban surface form. J Appl Meteorol 38:1261–1292

15. Coceal O, Thomas TG, Castro IP, Belcher SE (2006) Mean flow and turbulence statistics over groups of urban-like obstacles. Bound-Layer Meteorol 121:491-519

16. Takimoto H, Sato A, Barlow JF, Moriwaki R, Inagaki A, Onomura S, Kanda M (2011) Particle image velocimetry measurements of turbulent flow in outdoor and indoor urban scale models and flushing motions in urban canopy layers. Bound-Layer Meteorol 140:295–314

17. Coceal O, Goulart EV, Branford S, Thomas TG, Belcher SE (2014) Flow structure and near-field dispersion in arrays of building-like obstacles. J Wind Eng Ind Aerodyn 125:52-68

18. Belcher SE, Coceal O, Goulart EV, Rudd AC, Robins AG (2015) Process controlling atmospheric dispersion through city centers. J Fluid Mech 763:51-81

19. Huq P, Franzese P (2013) Measurements of turbulence and dispersion in three idealized urban canopies with different aspect ratios and comparisons with a Gaussian plume model. Bound-Layer Meteorol 147:103-121

20. Orlandi P, Leonardi S (2006) DNS of turbulent channel flows with two- and three-dimensional roughness. J Turbul 7. DOI: 10.1080/14685240600827526

21. Carpentieri M, Robins AG (2015) Influence of urban morphology on air flow over building arrays. J Wind Eng Ind Aerod 145:61-74

22. Salvati A, Coch Roura H, Cecere C (2017) Assessing the urban heat island and its energy impact on residential buildings in Mediterranean climate: Barcelona case study. Ener Build 146:38–54

23. Di Bernardino A, Monti P, Leuzzi G, Querzoli G (2015) Water-channel study of flow and turbulence past a two-dimensional array of obstacles. Bound-Layer Meteorol 155:73–85

24. Uehara K, Wakamatsu S, Ooka R (2003) Studies on critical Reynolds number indices for wind-tunnel experiments on flow within urban areas. Bound-Layer Meteorol 107:353–370
25. Monti P, Querzoli G, Cenedese A, Piccinini S (2007) Mixing properties of a stably stratified parallel shear layer. Phys Fluids 19:085104. DOI 10.1063/1.2756580
26. Corrsin S (1963) Estimates of the relations between Eulerian and Lagrangian scales in large Reynolds number turbulence. J Atmos Sci 20:115–119
27. Anfossi D, Rizza U, Mangia C, Degrazia GA, Pereira Marques Filho E (2006) Estimation of the ratio between the Lagrangian and Eulerian time scales in an atmospheric boundary layer generated by large eddy simulation. Atmos Environ 40:326–337
28. Wang QZ, Squires KD, Wu X (1995) Lagrangian statistics in turbulent channel flows. Atmos Environ 29:2417–2427
29. Guala M, Liberzon A, Tsinober A, Kinzelbach W (2007) An experimental investigation on Lagrangian correlations of small-scale turbulence at low Reynolds number. J Fluid Mech 574:405–427
30. Leonardi S, Orlandi P, Djenidi L, Antonia RA (2004) Structure of turbulent channel flow with square bars on one wall. Int. J Heat Fluid Flow 25:384–392
31. Michioka T, Sato A, Takimoto H, Kanda M (2011) Large-Eddy simulation for the mechanism of pollutant removal from a two-dimensional street canyon. Bound-Layer Meteorol 138:195–213
32. Salizzoni P, Marro M, Soulhac L, Grosjean N, Perkins RJ (2011) Turbulent transfer between street canyons and the overlying atmospheric boundary layer. Bound-Layer Meteorol 141:393–414
33. Badas MG, Querzoli G (2011) Spatial structures and scaling in the convective bound layer. Exp Fluids 50:1093–1107
34. Dallman A, Di Sabatino S, Fernando HJS (2013) Flow and turbulence in an industrial/suburban roughness canopy. Environ Fluid Mech 13:279–307
35. Cheng H, Castro IP (2002) Near wall flow over urban-like roughness. Bound-Layer Meteorol 104:229-259
36. Finnigan J (2000) Turbulence in plant canopies. Annu Rev Fluid Mech 32:519–571
37. Pelliccioni A, Monti P, Leuzzi G (2016). Wind-speed profile and roughness sublayer depth modelling in urban boundary layers. Bound-Layer Meteorol 160:225–248
38. Leonardi S, Castro IP (2010) Channel flow over large cube roughness: a direct numerical simulation study. J Fluid Mech 651:519-539
39. Jimenez J (2004) Turbulent flows over rough walls. Annu Rev Fluid Mech 36:173-196
40. Leonardi S, Orlandi P, Antonia RA (2007) Properties of d- and k-type roughness in a turbulent channel flow. Physics of Fluids 19:125101
41. Pasquill F (1974) Atmospheric diffusion, Wiley, New York, 429pp
42. Castro IP, Cheng H, Reynolds R (2006) Turbulence over urban-type roughness: deductions from wind-tunnel measurements. Bound-Layer Meteorol 118:109–131

43. Badas MG, Ferrari S, Garau M, Querzoli G (2017) On the effect of gable roof on natural ventilation in two-dimensional urban canyons. J Wind Eng Ind Aerod 162:24–34
44. Ferrari S, Badas MG, Garau M, et al (2017) The air quality in narrow two-dimensional urban canyons with pitched and flat roof buildings. International Journal of Environment and Pollution 62:347–368. DOI: 10.1504/IJEP.2017.089419
45. Garau M, Badas MG, Ferrari S, et al (2018) Turbulence and air exchange in a two-dimensional urban street canyon between gable roof buildings. Bound-Layer Meteorol 167:123–143
46. Di Bernardino A, Monti P, Leuzzi G, Querzoli G (2018). Pollutant fluxes in two-dimensional urban canopies. Urban Climate 24:80–93. DOI: 10.1016/j.uclim.2018.02.002
47. Reynolds RT, Castro IP (2008) Measurements in an urban-type boundary layer. Exp Fluids 45:141–156
48. Kanda M, Inagaki A, Miyamoto T, Gryschka M, Raasch S (2013) A new aerodynamic parametrization for real urban surfaces. Bound-Layer Meteorol 148:357–377
49. Poggi D, Katul G, Albertson J (2006) Scalar dispersion within a model canopy: measurements and three-dimensional Lagrangian models. Adv Water Resour 29:326–335
50. Hanna SR (1981) Lagrangian and Eulerian time-scale in the daytime boundary layer. J Appl Meteorol 20:242–249
51. Brunet Y, Finnigan JJ, Raupach MR (1994) A wind tunnel study of air flow in waving wheat: single-point velocity statistics. Bound-Layer Meteorol 70, 95-132
52. Foken T (2008) Micrometeorology. Springer

FIGURES

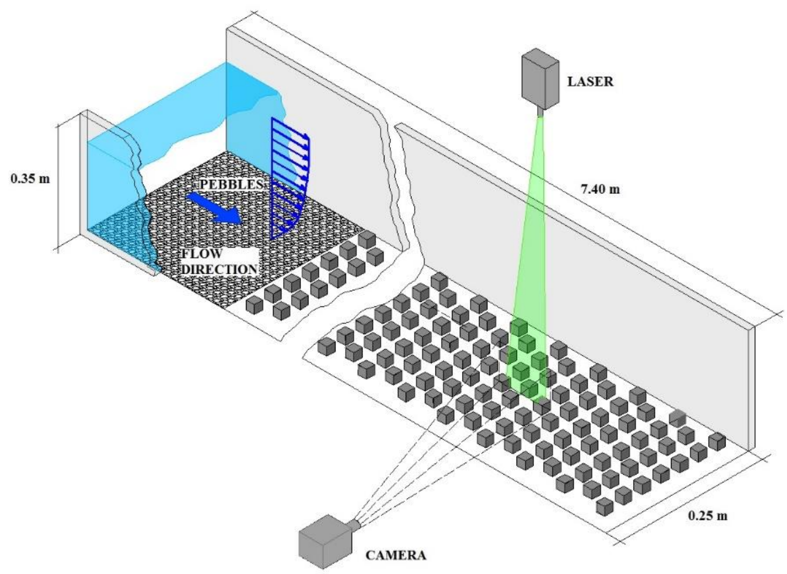

Fig. 1 Layout of the experimental setup for the Eulerian measurements (case $\lambda_P = 0.25$)

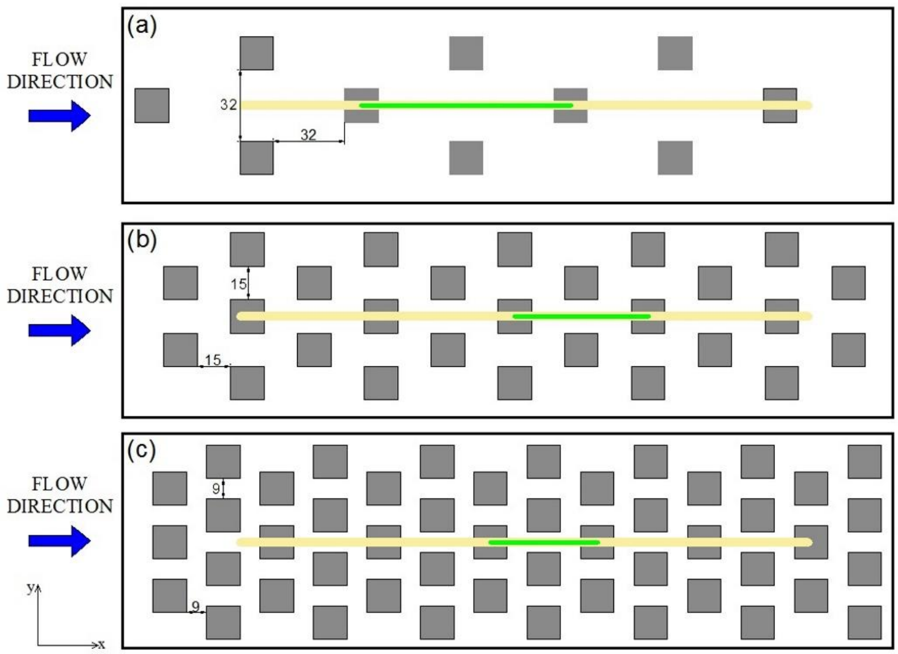

Fig. 2 Schematic plan view of the cube arrays for **a** $\lambda_P = 0.1$, **b** $\lambda_P = 0.25$ and **c** $\lambda_P = 0.4$. The green line is the signature along the horizontal plane of the vertical interrogation area used for the acquisition of the Eulerian variables, while the yellow line indicates that considered for the Lagrangian ones. The side of each cubical element is 15 mm. The streamwise and the spanwise directions are *x* and *y*, respectively. Measurements are in mm

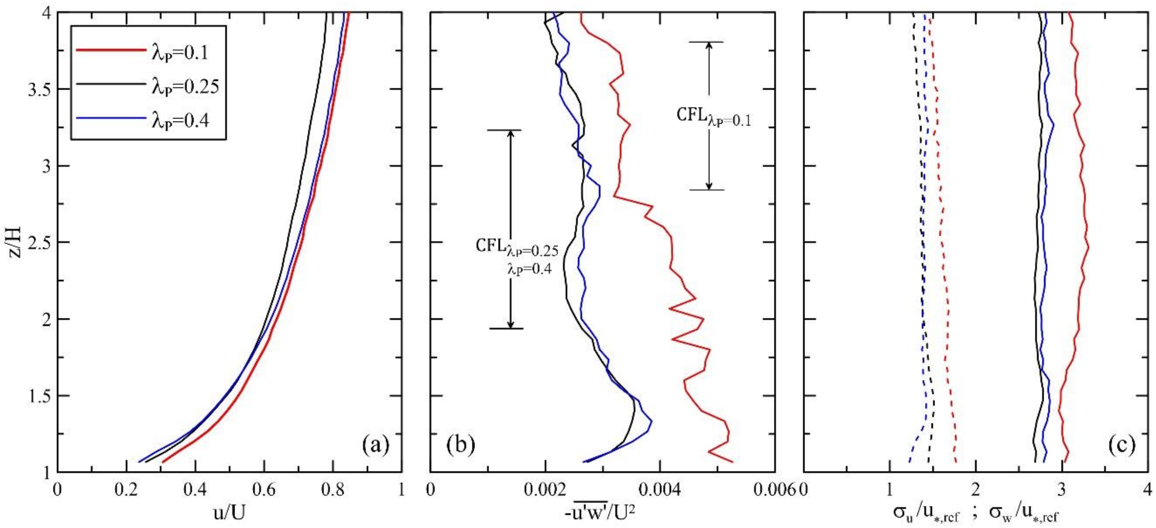

Fig. 3 Vertical profiles of normalized **a** streamwise mean velocity, **b** shear stress and **c** standard deviation of the streamwise (continuous lines) and vertical (dashed lines) velocity components for $\lambda_P = 0.1$ (red lines), $\lambda_P = 0.25$ (black) and $\lambda_P = 0.4$ (blue). The reference friction velocities calculated as the averages of the square root of the shear stresses in the CFL are $u_{*,ref}$ =0.0190 m s^{-1}, 0.0169 ms^{-1} and 0.0173 ms^{-1} for $\lambda_P = 0.1$, 0.25 and 0.4, respectively

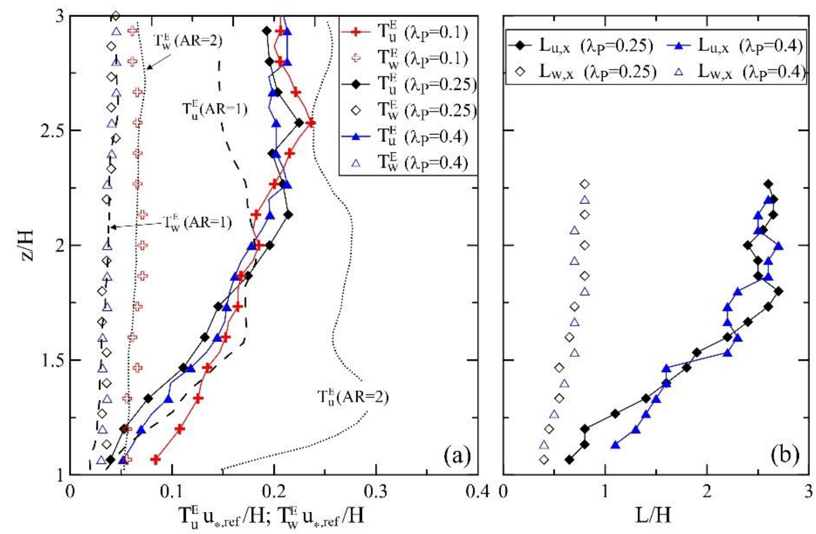

Fig. 4 a Vertical profiles of the non-dimensional Eulerian time scales of the turbulence. The vertical profiles of $T_u^E u_{*,ref}$ and $T_w^E u_{*,ref}$ found by Di Bernardino et al. (2017) [1] are also shown (dashed and dotted lines). **b** Vertical profiles of the Eulerian length scales $L_{u,x}$ (lines with symbols) and $L_{w,x}$ (symbols) normalized by the obstacle height for λ_P=0.25 and 0.4

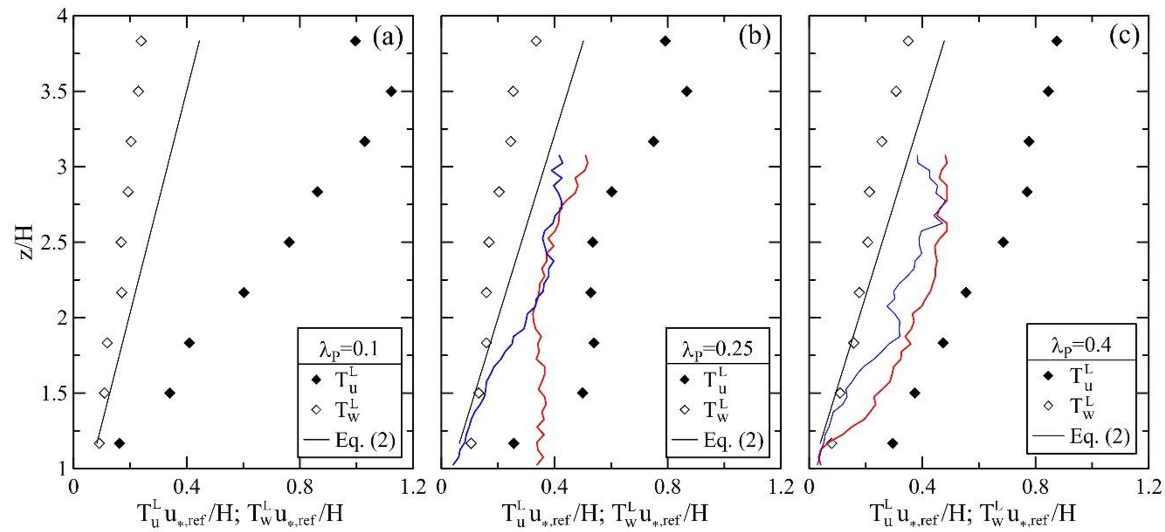

Fig. 5 Vertical profiles of the non-dimensional Lagrangian time scales estimated for **a** λ_P=0.1, **b** λ_P=0.25 and **c** λ_P=0.4. The continuous lines refer to $T_w^L u_{*,ref}/H$ calculated using Eq. (2) with (*z*-*d*) instead of *z*, where *d* is the displacement height. The red and blue lines indicate $T_u^L u_{*,ref}/H$ and $T_w^L u_{*,ref}/H$ for the 2D cases [1], respectively

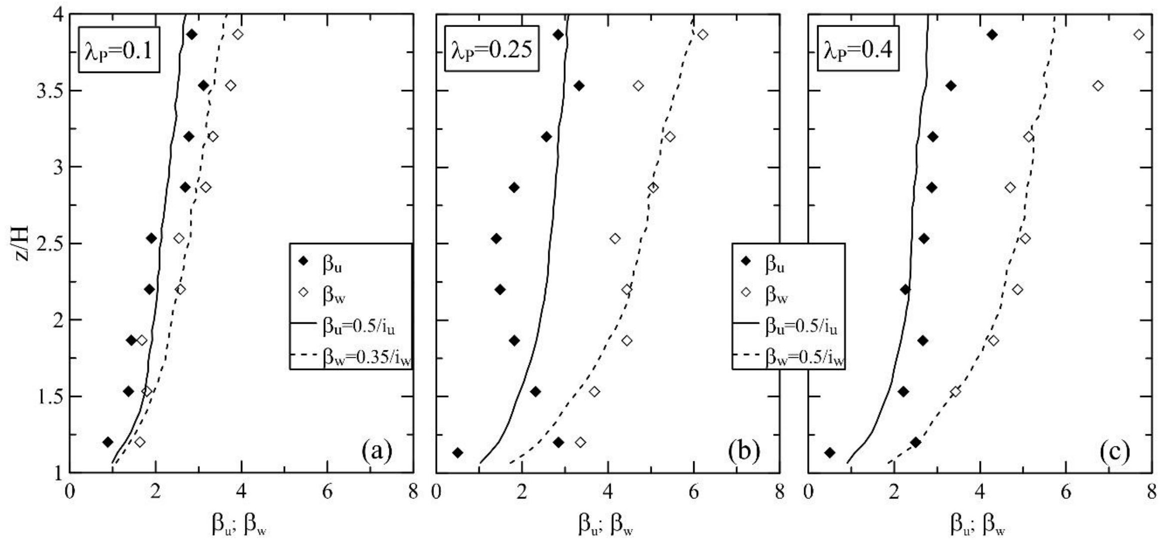

Fig. 6 Vertical profiles of $\beta_u = T_u^L/T_u^E$ and $\beta_w = T_w^L/T_w^E$ for **a** λ_P=0.1, **b** λ_P=0.25 and **c** λ_P=0.4. The continuous and dashed lines show Eq. (8) for β_u and β_w, respectively

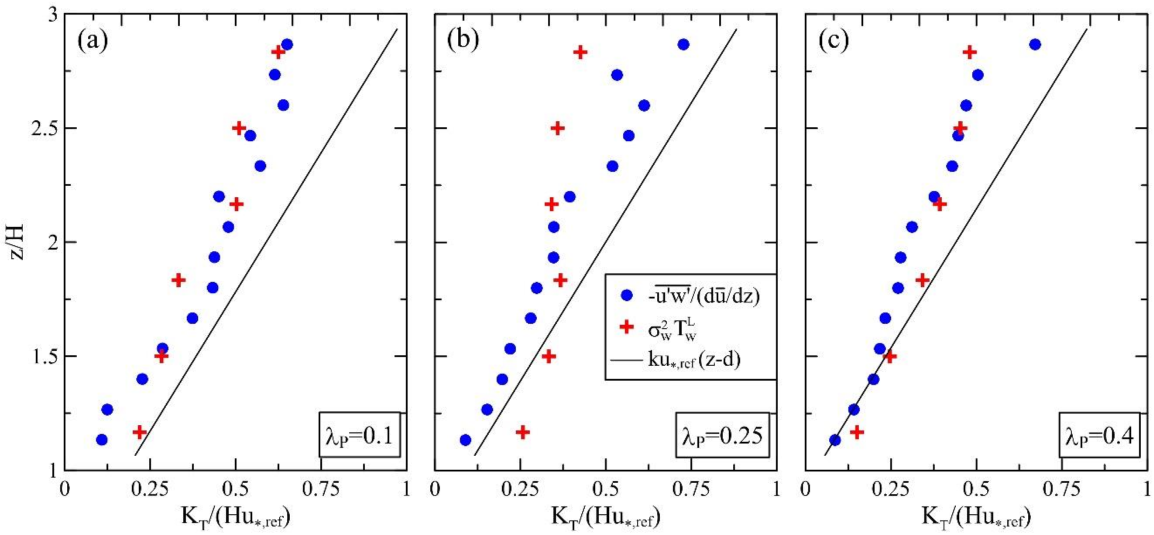

Fig. 7 Vertical profiles of the normalized turbulent diffusivity for **a** λ_P=0.1, **b** λ_P=0.25 and **c** λ_P=0.4. The values of the displacement height used in Prandtl's law are reported in Sec. 3.3